



Check for updates

RESEARCH ARTICLE

Subgrid modeling for compound flooding in coastal systems

Amirhosein Begmohammadi^a, Damrongsak Wirasaet^b, Ning Lin^a, J. Casey Dietrich^c, Diogo Bolster^b and Andrew B. Kennedy^b

^aDepartment of Civil and Environmental Engineering, Princeton University, Princeton, NJ, USA; ^bDepartment of Civil and Environmental Engineering and Earth Sciences, University of Notre Dame, Notre Dame, IN, USA; Department of Civil, Construction, and Environmental Engineering, North Carolina State University, Raleigh, NC, USA

ABSTRACT

Q1

10

15

20

25

02

Compound flooding, the concurrence of multiple flooding mechanisms such as storm surge, heavy rainfall, and riverine flooding, poses a significant threat to coastal communities. To mitigate the impacts of compound flooding events and improve preparedness, forecasts must represent the variability of flooding drivers over a wide range of spatial scales while still being timely. One approach to develop these forecasts is through subgrid corrections, which utilize information at smaller scales to "correct" water levels and current velocities averaged over the model scale. Recent studies have shown that subgrid models can improve both accuracy and efficiency; however, existing models are not able to account for the dynamic interactions of hydrologic and hydrodynamic drivers and their contributions to flooding along the smallest flow pathways when using a coarse resolution. Here, we have developed a solver called CoaSToRM (Coastal Subgrid Topography Research Model) with subgrid corrections to compute compound flooding in coastal systems resulting from fluvial, pluvial, tidal, and winddriven processes. A key contribution is the model's ability to enforce all flood drivers and use the subgrid corrections to improve the accuracy of the coarse-resolution simulation. The model is validated for Hurricane Eta 2020 in Tampa Bay, Florida. Improvements in prediction accuracy due to subgrid corrections are evaluated at 42 observation locations. The accuracy of the subgrid model with relatively coarse resolutions ($R^2 = 0.70$, 0.73, 0.77 for 3-, 1.5-, 0.75-km grid sizes) is much better than that of a standard counterpart (R² = 0.03, 0.14, 0.26 for 3-, 1.5-, 0.75km grid sizes). In this test, we observed that when comparing subgrid models with different resolutions, a 3-km subgrid simulation runs roughly 50 times faster than a 0.75-km subgrid simulation while maintaining the same level of accuracy.

ARTICLE HISTORY

Received 23 February 2024 Accepted 22 June 2024 Published online

KEYWORDS

Subgrid model: tropical cyclone; compound flooding; shallow water equation; numerical methods; semiimplicit discritization

1. Introduction

Compound flooding is a challenging issue due to the concurrence of coastal storm surge, intense precipitation, and river flooding. These processes occur at different temporal and spatial scales, encompassing storm surge, pluvial, and fluvial inundation. These processes have been simulated by two types of models: hydrologic models for rainfall collecting over watersheds and into channels, and hydrodynamic models for tides and surge from rivers to the open ocean. These models have been used separately or one-way coupled to study compound flooding in coastal regions (Chen et al. 2013; Cho et al. 2012; Dresback et al. 2013; Gori, Lin, and Smith 2020; Jin et al. 2017; Kerr et al. 2013; Wing et al. 2019). However, employing two models can create deficiencies in simulating interconnected processes. Hydrologic models lack the capability to address certain surface flow processes that interconnect with estuarine dynamics Zhang et al. (2020), and hydrodynamic models can exclude pluvial and fluvial processes Bilskie and Hagen (2018). A significant challenge is evident in the application of a tightly coupled or one comprehensive model to

represent the physical interactions between storm surge and rainfall-runoff (Santiago-Collazo, Bilskie, and Scott 2019). The implementation of full- and tight-coupling for such numerical models (e.g. hydrologic, ocean circulation, and hydraulic models) is much more intricate compared to loose- or one-way coupling. This complexity arises from the complicated mathematical representation of their physical processes, the computational power required, and the varying temporal and spatial resolutions (different time and length scales) of the numerical models (Santiago-Collazo, Bilskie, and Scott 2019).

Recently, Zhang et al. (2020) presented a creek-toocean 3D baroclinic model based on SCHISM (Semiimplicit Cross-scale Hydroscience Integrated System Model) that aims to unite hydrologic and hydrodynamic models in a single modeling platform to simulate compound floods. They simulate Hurricane Irene's impact on Delaware Bay as an example with spatial resolution down to 20 m. The streamflow from hydrologic models (e.g. NOAA's National Water Model (NWM)) is injected into the SCHISM grid at the intersections of NWM's segments and SCHISM's land

70

135

145

Q3

155

165

175

180

boundary, and thus the pluvial and fluvial processes are directly handled by SCHISM. They showed the model's accuracy, stability, and robustness with a focus on the compound flooding events. Separately, SFINCS, a new solver to compute compound flooding in coastal systems due to fluvial, pluvial, tidal, wind- and wave-driven processes in a computationally efficient way, was introduced and validated for various application scenarios (Leijnse et al. 2021). The model uses simplified equations for mass and momentum, influenced by storm surge and wave boundary conditions, as well as precipitation rates and upstream river discharges. In the case study of Hurricane Irma's impact on Jacksonville (Florida, USA), the observed flooding was found to be a result of a combination of fluvial, pluvial, tidal, and winddriven flooding. Like many numerical models, these recent models are faced with trade-offs between accuracy and efficiency. High accuracy requires high levels of spatial resolution, which entails significant computational costs, posing a challenge for these models in conducting large-scale simulations. On the other hand, models utilizing coarser resolutions are unable to account for the dynamic interactions of hydrologic and hydrodynamic drivers and their contributions to flooding along the smallest flow pathways, leading to lower accuracy.

A potential and promising approach to develop cost-effective and accurate models involves the use of subgrid corrections. These models have gained significant attention in various research domains, particularly in the study of flow over tidal flats and wetlands, urban flooding, and storm surge applications (Casulli 2009; Defina 2000; Kennedy et al. 2019; Nederhoff et al. 2024; Sanders, Schubert, and Gallegos 2008; Wu et al. 2016). The basic idea of a subgrid method is to account for small-scale processes that cannot be resolved by the main computational grid. These models enhance the overall accuracy of the simulations while keeping computational costs manageable. Previous studies have examined using subgrids for modeling surge, inundation, and circulation (Casulli 2009; Casulli and Stelling 2011; Defina 2000; Kennedy et al. 2019).For instance, Neal, Schumann, and Bates (2012) used the subgrid concept to present a new hydraulic model for efficiently simulating dynamics of water surface elevation, wave speed, and inundation extent over large areas. It extends LISFLOOD-FP (Bates and De Roo 2000) to include subgrid-scale channels, improving accuracy in simulating river behavior. The model has been successfully applied in various flood modeling scenarios (Bates et al. 2021; Y. Zhang and Reza Najafi 2020). Most of the subgrid studies focused on corrections of the mass conservation equation, where they account for the variation of the bathymetry in a coarse grid to deal with partially wet cells (Casulli 2009; Casulli and Stelling 2011; Defina 2000). J. Woodruff et al (2023,

2021). integrated subgrid corrections into the ADCIRC (ADvanced CIRCulation) model (Luettich et al. 1992), a finite element-based hydrodynamic solver, to improve its accuracy when operating on a coarse mesh. Similarly, Begmohammadi et al. (2023) demonstrated the implementation of subgrid corrections in the SLOSH Jelesnianski (1992) storm surge model, leading to significant improvements in model accuracy without substantially increasing computational costs (Begmohammadi, 2022). The HEC-RAS model is another well-known finite-volume-based hydrodynamic model (Brunner 2016). A so-called subgrid bathymetry approach is also implemented on the model. To consider the subgrid approach, the model calculates hydraulic radius, volume, and cross-sectional data for each cell using the finer resolution data. Overall, these models ignored the additional effects that comes from the momentum conservation equations. Volp, Van Prooijen, and Stelling (2013) used a finite volume technique to correct the momentum equation with the assumption of simplified canonical flow (a channel flow with a uniform flow and constant friction slope) over a coarse grid. They developed corrections for bottom friction and advection terms, which can be significant in specific scenarios, such as channel flows characterized by a large variation in topography. Kennedy et al. (2019) developed shallow water subgrid systems based on a volume averaging technique (Whitaker 1998) that are similar to previous studies, but have additional terms and closures that had been neglected and arise from the averaging process from the mass and momentum conservation equations. The numerical scheme that has been used for these subgrid models is another important aspect that affects the efficiency of the model especially the discretization momentum conservation equations. Momentum equations can be discretized in either a semi-implicit or explicit manner. In the semi-implicit method, hydrostatic pressure and bottom friction terms, as demonstrated in the SCHISM model (Y. Zhang and Baptista 2008), can be treated implicitly, resulting in a more complex solution algorithm. This semi-implicit discretization permits the use of larger time steps, leading to significant gains in computational efficiency.

In this study, we present a subgrid-based model for compound flood modeling in coastal systems due to fluvial, pluvial, tidal, and wind-driven processes. We adopt the subgrid model presented by Kennedy et al. (2019) and incorporate key factors such as wind stress, gradient of atmospheric pressure, spatial varying precipitation, infiltration, bottom friction, river discharges, and river surface elevations as boundary conditions to the model. Subsequently, we integrate subgrid corrections to enhance the accuracy of these parameters. Two-dimensional upscaled shallow water equations (in which a volume averaging technique Whitaker

260

265

270

(1998) is applied on the computational grids to consider coarse grid quantities) are discretized semi-implicitly, whereas hydrostatic pressure gradient and bottom friction terms are discretized fully implicitly. This semi-implicit discretization allows for larger time steps, which can lead to significant computational efficiency gains Casulli (1990). It also offers a greater numerical stability compared to explicit methods. This stability is especially beneficial when simulating complex and rapidly changing flow patterns Casulli (1990). The model's validation was conducted for Hurricane Eta in 2020, specifically in Tampa Bay, Florida, USA.

2. Methodology

2.00

220

225

230

2.1. Governing equations

Generally, two-dimensional shallow water equations (SWEs) are used to model flows in coastal and environmental engineering scenarios, including estuarine circulation, tides, and storm surges (Canestrelli and Toro 2012; Dresback, Kolar, and Casey Dietrich 2005; Luettich et al. 1992). Here, we adopt the SWE-based subgrid model proposed by Kennedy et al. (2019) with additions for wind stress, gradient of atmospheric pressure, spatially varying precipitation, infiltration, bottom friction, and river discharges. Upscaled equations are 215 derived by applying averaging technique Whitaker (1998) to the non-conservative form of SWEs.

2.1.1. Upscaled equations

The upscaled mass conservation equation with additional source terms to incorporate precipitation and infiltration is as follows:

$$\frac{\partial \mathcal{V}_{w}(\langle \boldsymbol{\eta} \rangle)}{\partial t} + \frac{\partial \langle \boldsymbol{H} \rangle \langle \boldsymbol{U} \rangle}{\partial \mathbf{x}} + \frac{\partial \langle \boldsymbol{H} \rangle \langle \boldsymbol{V} \rangle}{\partial \mathbf{v}} = \langle \boldsymbol{R} \rangle - \langle \boldsymbol{I} \rangle \quad (1)$$

The symbols enclosed by $\langle \cdot \rangle$ brackets represent values averaged over the grid, with the exception of velocity. $V_{w}(\langle \eta \rangle)$ represents the wet volume per unit area, corresponding to a specific wet-averaged surface elevation $\langle \eta \rangle$. The symbol $\langle U \rangle$ denotes the averaged velocity vector at the grid level, calculated through the equation $\langle U \rangle = {}^{R} HUdV/{}^{R} HdV$, where $\langle H \rangle$ signifies the gridaveraged water depth. The terms $\langle R \rangle$ and $\langle I \rangle$ refer to the volume of precipitation and infiltration within a given cell, respectively.

Infiltration is a significant factor in modeling inland flooding by influencing how water moves through soil and interacts with the ground surface during heavy rainfall events. Although there are different categories of infiltration models (Mishra and Singh 1999; Rawls et al. 1992), here we implemented a temporally constant, spatially varying infiltration, which showed promising results for compound flood modeling (Gori, Lin, and Smith 2020; Leijnse et al. 2021; Sarhadi et al. 2024).

The model has the potential to incorporate more sophisticated infiltration methods in future updates. Note that the current version requires hourly time series data of spatially varying precipitation on the computational grid as an input.

The upscaled momentum conservation equations 245 with additional forces in x and y directions are:

$$\langle H \rangle \frac{\partial \langle U \rangle}{\partial t} - \langle U \rangle \nabla \cdot (\langle U \rangle \langle H \rangle) + \frac{\partial}{\partial x} (\mathcal{C}_{UU} \langle U \rangle \langle V \rangle \langle H \rangle)$$

$$+ \frac{\partial}{\partial y} (\mathcal{C}_{UV} \langle U \rangle \langle V \rangle \langle H \rangle)$$

$$= -g \langle H \rangle \left(\mathcal{C}_{\eta,xx} \frac{\partial \langle \eta \rangle}{\partial x} + \mathcal{C}_{\eta,xy} \frac{\partial \langle \eta \rangle}{\partial y} \right)$$

$$- \phi |\langle U \rangle | \left(\mathcal{C}_{M,fxx} \langle U \rangle + \mathcal{C}_{M,fxy} \langle V \rangle \right)$$

$$- \frac{\langle H \rangle}{\rho} \frac{\partial P_A}{\partial x} - f_c \langle H \rangle \langle V \rangle + \frac{\phi \langle \tau_{sx} \rangle}{\rho_{gir}}$$

$$(2)$$

$$\langle H \rangle \frac{\partial \langle V \rangle}{\partial t} - \langle V \rangle \nabla \cdot (\langle U \rangle \langle H \rangle)$$

$$+ \frac{\partial}{\partial x} (\mathcal{C}_{VU} \langle V \rangle \langle U \rangle \langle H \rangle) + \frac{\partial}{\partial y} (\mathcal{C}_{VV} \langle V \rangle \langle U \rangle \langle H \rangle)$$

$$= -g \langle H \rangle \left(\mathcal{C}_{\eta,yx} \frac{\partial \langle \eta \rangle}{\partial x} + \mathcal{C}_{\eta,yy} \frac{\partial \langle \eta \rangle}{\partial y} \right) - \phi |\langle U \rangle|$$

$$\left(\mathcal{C}_{M,fyx} \langle U \rangle + \mathcal{C}_{M,fyy} \langle V \rangle \right) - \frac{\langle H \rangle}{\rho} \frac{\partial P_A}{\partial y}$$

$$+ \langle H \rangle f_c \langle U \rangle + \frac{\phi \langle \tau_{sy} \rangle}{\rho_{air}}$$

$$(3)$$

In Equations (2)–(3), the term $=A_w/A_G$ represents the wet area fraction; the coefficients C_{UU} , C_{UV} , C_{VU} , C_{VV} are subgrid corrections to nonlinear convection terms; C_n is the subgrid correction for the surface gradient; and C_M is the subgrid correction for effective bottom stress. All these coefficients come from the volume averaging technique (see Kennedy et al. (2019)). Terms P and τ_s indicate the atmospheric pressure and storm-induced wind stress, respectively. To account for wind stress, we employ a variable wind drag coefficient, which depends on the wind speed (Powell and Ginis 2006). To transfer the wind stress into the momentum equations within the upscaled SWEs, the sea-surface momentum stress similar to the ADCIRC model $au_w =
ho C_{Deag} U_{10}^2 \quad \Gamma =
ho C_{Drag} U_{10}^2 \% Math Type! End! 2! 1!
ho_{air}$ (Luettich et al. 1992) is used. Where U_{10} and ρ denote the wind speed at the elevation of 10 m above the sea surface and reference air density, respectively. C_{Draa} represents the wind drag coefficient. This coefficient, as proposed by Garratt Garratt (1977), is given by $C_{\text{Drag}} = \frac{1}{1000} \left(\frac{15}{20} + \frac{40}{600} U_{10} \right)$. Note that the model enforces a maximum limit on the wind drag coefficient, setting it at $C_{Drag} = 0.002$.

To solve these equations, closures for determining the subgrid correction parameters are proposed in Kennedy et al. (2019). Here, we focus on correcting the fractional wetting and drying within the grid cell. We also correct the atmospheric pressure, storminduced wind stress, and bottom roughness. However, it does not address complex subgrid corrections for advection and surface gradient terms. Specifically, the subgrid coefficients are set as $C_{UU} = C_{V\ V} = C_{UV} = C_{V\ U} = 1$ (convective terms coefficients), $C_{\eta,xx} = C_{\eta,yy} = 1, C_{\eta,xy} = C_{\eta,yx} = 0$ (surface gradient coefficients). For the Manning friction coefficient, $CM,f,xx = CM,f,yy = \langle Cf \rangle G,CM,f,xy = CM,f,yx = 0$. Note that Manning's formula is used to approximate the friction $C_{fG} = \frac{gn^2}{H^{1/3}}$, where n denotes the

Manning's roughness coefficient and $g = 9.81 \text{ m/s}^2$ is gravitational acceleration.

2.2. Discretization

285

290

295

The system of upscaled equations, given by (1)-(3), involves three unknowns: $\langle \eta \rangle$, $\langle U \rangle$, and $\langle V \rangle$. It's important to note that the averaged water depth $\langle H \rangle = V_w$ is a predetermined variable derived from $\langle \eta \rangle$ and a specified digital elevation model b(x,y). These equations are discretized on a staggered C-grid Arakawa and Lamb (1977) (refer to Figure 1). The unknown variable $\langle \eta \rangle$ is positioned at the cell-center, while $\langle U \rangle$ and $\langle V \rangle$ are situated at the midpoint of the vertical and horizontal cell edges, respectively. The discretization is performed using a semi-implicit finite difference method. The advection component in Equations (2) and (3) is discretized through an explicit upwind scheme. To allow the model to perform with the larger Δt , the surface gradient and bottom stress components in the momentum equations, along with the velocities

in the continuity Equation (1), are treated implicitly. Henceforth, for the sake of simplicity, we substitute $\langle \eta \rangle$, $\langle U \rangle$, $\langle V \rangle$, $\langle H \rangle$, $\langle R \rangle$, and $\langle I \rangle$ with η , u, v, H, R, and I.

305

For each cell edge, a semi-implicit discretization of the momentum equations is carried out in the *x*- and *y*-directions at the vertical and horizontal edges, respectively:

$$u_{i+\frac{1}{2}j}^{n+1} = \frac{1}{H_{i+\frac{1}{2}j}^{*}}$$

$$\left[H_{i+\frac{1}{2}j}^{n} u_{i+\frac{1}{2}j}^{n+1} - \Delta t F_{i+\frac{1}{2}j}^{n} - g \frac{\Delta t}{\Delta x} H_{i+\frac{1}{2}j}^{n} \left(\eta_{i+\frac{1}{2}j}^{n+1} - \eta_{i+\frac{1}{2}j}^{n+1} \right) \right]$$

$$+ \frac{\Delta t}{H_{i+\frac{1}{2}j}^{*}}$$

$$\left[\frac{H_{i+\frac{1}{2}j}^{n}}{\rho_{air} \Delta x} \left(P_{i+1,j}^{n+1} - P_{i,j}^{n+1} \right) - f_{c} H_{i+\frac{1}{2}j}^{n} v_{i+\frac{1}{2}j}^{n} + \frac{\phi_{i+\frac{1}{2}j}^{n}}{\rho_{air} \Delta x} \tau_{i+\frac{1}{2}j}^{n+1} \right],$$

$$(4)$$

and $v_{i,j+\frac{1}{2}}^{n+1} = \frac{1}{H_{i,j+\frac{1}{2}}^*}$ $\left[H_{i,j+\frac{1}{2}}^n v_{i,j+\frac{1}{2}}^{n+1} - \Delta t G_{i,j+\frac{1}{2}}^n - g \frac{\Delta t}{\Delta y} H_{i,j+\frac{1}{2}}^n \left(\eta_{i,j+1}^{n+1} - \eta_{i+\frac{1}{2}j}^{n+1}\right)\right] + \frac{\Delta t}{H_{i+\frac{1}{2}j}^*}$ $\left[\frac{H_{i,j+\frac{1}{2}}^n}{\rho_{air}\Delta y} \left(P_{i,j+1}^{n+1} - P_{i,j}^{n+1}\right) - f_c H_{i,j+\frac{1}{2}}^n v_{i,j+\frac{1}{2}}^n + \frac{\phi_{i,j+\frac{1}{2}}^n}{\rho_{air}\Delta x} \tau_{i,j+\frac{1}{2}}^{n+1}\right],$ (5)

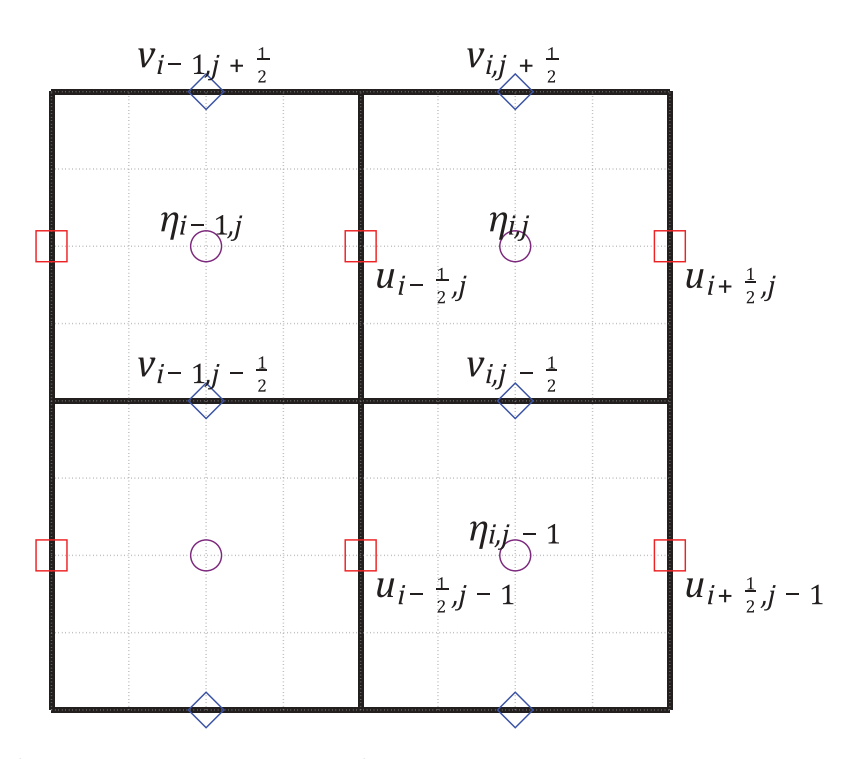


Figure 1. Depiction of the staggered C-Grid layout. Surface elevation (η) is denoted by purple circles at the centers of cells. Horizontal velocity (u) is represented by red squares, positioned at the vertical edges' midpoints. Vertical velocity (v) is illustrated with blue diamonds, located at the midpoints of the horizontal edges.

375

380

395

where $G_{i,j+\frac{1}{2}}$ and $F_{i+\frac{1}{2},j}$ denote the discretization of the advection terms (see Kennedy et al. (2019) for more details) and H* define as follows:

$$\begin{split} H_{i+\frac{1}{2}j}^* &= \frac{1}{H_{i+\frac{1}{2}j}^n + \Gamma_{i+\frac{1}{2}j}\Delta t}, H_{ij+\frac{1}{2}}^* = \frac{1}{H_{i,j+\frac{1}{2}}^n + \Gamma_{i,j+\frac{1}{2}}\Delta t}, \\ \text{and, } \Gamma^{i+\frac{1}{2},j} &= \langle C_f \rangle_G \times \left| \sqrt{u_{i+\frac{1}{2}j}^2 + v_{i+\frac{1}{2}j}^2} \right|. \text{ Note that } u_{i+\frac{1}{2},j} \end{split}$$

315

320

represents the average velocity computed from the four surrounding v velocities. The same approach is applied to calculate $\Gamma^{i+\frac{1}{2}j}$.

For each cell, the discretization of continuity Equation (1) with the Euler backward time discretization is:

$$\frac{V_{w}\left(\eta_{i,j}^{n+1}\right) - V_{w}\left(\eta_{i,j}^{n}\right)}{\Delta t} + \frac{1}{\Delta x} \left[\sum_{s \in E\left(i + \frac{1}{2}j\right)} u_{i + \frac{1}{2}j}^{s,n+1} H_{i + \frac{1}{2}j}^{s,n} - \sum_{s \in E\left(i - \frac{1}{2}j\right)} u_{i - \frac{1}{2}j}^{s,n+1} H_{i - \frac{1}{2}j}^{s,n} \right] + \frac{1}{\Delta y} \left[\sum_{s \in E\left(i,j + \frac{1}{2}\right)} u_{i,j + \frac{1}{2}}^{s,n+1} H_{i,j + \frac{1}{2}}^{s,n} - \sum_{s \in E\left(i,j - \frac{1}{2}\right)} u_{i,j - \frac{1}{2}}^{s,n+1} H_{i,j - \frac{1}{2}}^{s,n} \right] \\
= R_{i}^{n} - I_{i}^{n} \tag{6}$$

where $V_w(\eta_{i,j})$ represents the volume per unit cell area

The approximate solutions for η^{n+1} , u^{n+1} , and v^{n+1} are obtained by solving a system of equations derived by inserting the discretized momentum equations into Equation (6) as detailed in Casulli (2009). This leads to a set of slightly nonlinear algebraic equations, simply expressed as follows:

$$\mathbf{V}(\eta^{n+1}) + \mathbf{T}\eta^{n+1} = \mathbf{b} \tag{7}$$

where η^{n+1} represents the solution at the next time level, while the matrix **T** emerges from the substitution process. Additionally, V denotes the water volume vector, and **b** signifies the known vector on the righthand side. Notably, the matrix **T** is symmetrical, featuring positive diagonal elements and negative off-diagonal elements. This system of (mildly) nonlinear equations is addressed using the Newton-Raphson method to determine η^{n+1} . Following this, the velocities at time level n + 1 are computed through back substitution using the now-established η^{n+1} . We refer to Kennedy et al. (2019) for more detailed account of the numerical method.

To minimize the computational cost, a pre-storage lookup table is utilized in order to store the cell volume and wet area as a function of surface elevations. These tables can be generated for all cells in an initial preprocessing process. Note that the basic model (without wind stress, atmospheric pressure gradient, river discharge, precipitation, and infiltration) is validated for various benchmark problems Begmohammadi et al. (2021); Kennedy et al. (2019). The discharge from the rivers can be imposed as fluxes or surface elevation boundary conditions at any point within the computational domain.

2.3. Subgrid connectivity

Incorporating subgrid modeling to address unresolved topography in SWEs enables the use of larger grid cells for computational efficiency. However, employing overly large grid cells can result in artificial crossflows between areas that are hydraulically separated by physical barriers (e.g. a dune crest or raised highway) smaller than the grid size. Various methods have been used to address the subgrid surface connectivity, such as mesh refinement and edge blocking approaches (Hodges 2015; Li and Hodges 2019; Platzek et al. 2016). Casulli (2019) introduced a cell clone approach that eliminates artificial cross-flows between disconnected regions within a cell without need for additional mesh Begmohammadi et al. (2021) extended this approach by breaking the cell clone into sub-clones. This modification removes cross flows when barriers within the coarse grids are submerged, effectively handling the storm surge scenario.

Here, a simple method is used to represent the effects of the barriers and blockage on the coarse grid. First, the cells with barriers are identified. Second, the height of the barrier is determined by checking for the disconnected wet areas in a specific range of water surface elevations. Third, the heights of these barriers are mapped on the cell edges. These three steps are done before the simulation.

3. Results

3.1. Hurricane eta in 2020

Tampa Bay, located on the west Florida coast, encompasses Pinellas, Hillsborough, and Manatee Counties, with Pinellas and Hillsborough being densely populated. Despite being the fourth-largest U.S. port in tonnage, the bay faces potential vulnerability to storm surge due to its geographical features, surrounded by low-lying lands and impacted by surgeinduced edge waves trapped on the west Florida shelf (Lin and Emanuel 2016; Weisberg and Zheng 2006; Yankovsky 2009). Tampa Bay has been fortunate to avoid major hurricanes since 1921, and historical records indicate fewer storms track into this region compared to the U.S. coasts along the Atlantic or farther west in the Gulf of Mexico.

However, the region was impacted significantly by Hurricane Eta in 2020. Eta originated from a tropical wave off the west coast of Africa, intensifying into

a category 4 hurricane before making landfall in Nicaragua. After crossing Central America, Eta reemerged in the Gulf of Honduras, regaining tropical storm status and subsequently making landfall in the Florida Keys (Figure 2). The system then turned northnortheastward and made landfall near Cedar Key, Florida, at around 0900 UTC at November 12, with its maximum winds weakening to nearly 23.15 m/s due to strong west-southwesterly shear and some intrusion of dry air Pasch et al. (2021).

Eta caused inundation levels of 0.92 to 1.22 m above ground level in the Tampba Bay region (Pasch et al. 2021). Tide gauges from the National Ocean Service (NOS) recorded peak water levels of 1.19 m above Mean Higher High Water (MHHW) at Old Port Tampa and Tampa-East Bay, and 1.07 m MHHW in St. Petersburg. Stream gauges from the United States Geological Survey (USGS) further confirmed these heights, with examples such as 1.25 m 420 MHHW recorded on Lake Seminole in Pinellas County and 1.16 m MHHW on the Hillsborough River in Tampa (Pasch et al. 2021). In addition, Hurricane Eta caused substantial rainfall in the 425 greater Tampa Bay region, with multiple locations reporting rainfall exceeding 0.20 m. The highest amount recorded was 0.27 m near Sun City Center in Hillsborough County. Flooding was reported far inland, near the Manatee River and Alafia River. The peak of the flood upstream of the Manatee River 430 was recorded around 12 November at 22:00, reaching a height of 4 m (Manatee River at SR 64 near Mayakka Head, FL USGS gauge 0299950). In the closest coastal gauge to the Manatee River, the flood peaked around 12 November at 4:00, measuring approximately 1.25 m (NOAA tide and current gauge 8,726,384) Pasch et al. (2021). This indicates that the runoff-driven streamflows caused flooding later than the ocean-driven surge. This flooding led to significant impacts in the greater Tampa Bay area. In Pinellas County, 33 individuals were rescued from flooded homes and stranded vehicles in Passa-Grille, while other areas between St. Pete Beach and Madeira Beach faced inundation of up to a meter from storm surge. The storm also caused several sailboats to break free of their moorings, leading to some being stuck under a bridge or beached in Gulfport (Pasch et al. 2021). Coastal areas in Hillsborough, Manatee, Sarasota, Charlotte, 450 and Lee Counties experienced street flooding and road closures. More than 40,000 customers lost power in the greater Tampa Bay area (Pasch et al. 2021). Given the substantial impacts of Hurricane Eta, and especially its combined effects from storm surge and rainfall-induced flooding, this study aims to evaluate the performance of the CoaSToRM model in simulating the compound flooding from Eta on the greater Tampa Bay area.

3.2. Model setup

To simulate compound flooding using CoaSToRM for the case of Hurricane Eta in Tampa Bay, two-step nested models were set up. For the large-scale simulation of Eta's effects on offshore water levels, we use the ADvanced CIRCulation (ADCIRC) model (Luettich et al. 1992), which is a well-known, finite-element-based, storm surge model. Its grid includes 376,814 elements and 221,706 nodes, and it covers the western north Atlantic Ocean, Caribbean Sea, and Gulf of Mexico (Figure 3). The large-scale model is forced by tidal data obtained from a global model (TPXO8-ATLAS Egbert and Erofeeva (2002)), and by surface wind and pressure fields obtained from a parametric wind model (Holland vortex (Holland 1982)) based on best-track information from Eta. To consider the wave effects, the ADCIRC model is coupled with SWAN (Dietrich et al. 2011).

470

475

480

495

500

505

For the regional simulation of Eta's effects on compound flooding, we use the CoaSToRM model. Topographic and bathymetric data for the Tampa Bay region were obtained at 3-m horizontal resolution from the NOAA Digital Coast (CIRES, 2014) (CIRES). All topographic and bathymetric elevations, and all waterlevel data herein, are relative to the North American Vertical Datum of 1988 (NAVD88) Zilkoski, Richards, and Young (1992). A spatially-varying roughness is used based on land elevation for Research in Environmental Sciences (CIRES). The high-resolution bathymetric data with 660,000,000 pixels is shown in Figure 3. As the focus of this paper is the performance of the subgrid model at coarser resolutions, we consider three coarse grids with 30×22 ($\Delta x = \Delta y = 3$ km), $60 \times 44 \ (\Delta x = \Delta y = 1.5 \text{ km}), \text{ and } 120 \times 88$

 $(\Delta x = \Delta y = 0.75 \text{ km})$ cells, respectively. We also ran simulations with the same resolution without the subgrid for all three grids. The high-resolution bathymetric data are used to compute pre-storage lookup tables (the cell volume and wet area as a function of surface elevations)

The ADCIRC+SWAN model was run for 7 days of simulations from November 7th to 14th. The CoaSToRM model was run for 3 days from November 11th to 13th. Water surface elevations at the ocean boundary condition of the CoaSToRM model are obtained from the large-scale ADCIRC+SWAN simulation. The initial water level for the CoaSToRM model are set to a constant 0.28 m above mean sea level. This adjustment accounts for the 0.12-m correction to the NAVD88 datum in Tampa Bay, as well as the 0.16-m correction for the seasonal mean sea level variability observed in the region during November. The parametric model Holland (1982) is used to generate surface wind and pressure fields due to Eta. Precipitation forcing is supplied by NCEP/EMC with 4 km resolution (Du 2011) to the computational grid.

585

605

610

625

Water level boundary conditions (for Manatee River) and river fluxes (for Alafia River, Tampa Bypass Canal) for rivers are obtained from USGS (U.S. Geological Survey, n.d.).

3.3. Predictions of coastal water levels

To evaluate the model's performance, we compared 520 the water surface elevations computed by the subgrid model with the observed time-series data from NOAA (National Oceanic and Atmospheric Administration, n. d..) stations. These gauges are located near the coast-525 line of Tampa Bay and are depicted in Figure 2.

During Hurricane Eta, the model predicted storm surge levels in the Tampa Bay area of Florida, ranging from 1 to 1.45 m above the North American Vertical Datum of 1988 (NAVD88), aligning well with observational data. The model predicted water levels at the National Ocean Service (NOS) tide gauges in Old Port Tampa and TampaEast Bay in the northern part of the bay, recording peak water levels of around 1.4 and 1.3 m above NAVD88, while St. Petersburg's NOS gauge documented a peak water level of 1.25 m above NAVD88. These values closely match the observed data, with an underestimation error of less than 0.05 in Old Port Tampa. However, our model employs a coarse grid, which may contribute to inaccuracies in predicting water levels.

535

540

555

We evaluated the subgrid model performance across different grid resolutions to investigate how the model's accuracy changes as the resolution is increased. For these simulations, we accounted for all driving forces, including ADCIRC+SWAN boundary conditions, wand and atmospheric pressure fields, precipitation and infiltration, and river water discharges. The time series of water surface elevations are presented in Figure 4 for three resolutions utilizing the subgrid model. The E_{RMS} values, as shown in Table 1, remain almost identical across all grid resolutions for all selected gauges near to the coastline. This indicates that the subgrid model is not sensitive to these changes in grid resolution.

The coastal water-level observations can be used to examine the relative effects of (a) model forces, including both hydrodynamic and hydrological inputs; and (b) model resolution, including the benefits of the subgrid corrections. For the model forces, we considered simulations using the coarsest grid resolution ($\Delta x = 3$ km). There are three distinct simulations conducted as follows: (1) the model is forced with boundary conditions from ADCIRC +SWAN; (2) meteorological forces, including wind and atmospheric pressure fields, are added to the model from simulation 1 (BC+Meteo); and (3) precipitation and infiltration are added to the model from simulation 2 along with river water discharges (All Forces). Lastly, a fourth run is executed with all Forces above without the subgrid implementation, where the model is run with the cell-averaged bathymetric elevation, aiming to observe the specific effect of the subgrid model on the results (Standard Solution All Forces).

The time series of surface elevation for two gauges inside the bay, obtained using the coarsest grid $(\Delta x = \Delta y = 3km)$, are presented in Figure 5. These results help illustrate the relative contribution of each process across the domain. To quantify the model's performance, we use root-mean-square errors (E_{RMS}) over 60 hours of simulations. The E_{RMS} values are reported in Table 1. It can be seen that the E_{RMS} values for simulation 2 (BC+Meteo) are smaller than the model 1 (BC) with only boundary conditions. It can be concluded that wind and atmospheric pressure has a large effect on the modeled water levels, where the peak of the surge are much closer to the observation when meteorological forces included (simulation 2). Incorporating precipitation and infiltration into the model leads to a slight improvement in accuracy. This enhancement can be seen in stations 2, and 4, as illustrated in Figure 5 and Table 1. In general, when we compare the impact of meteorological forces and precipitation on the peak water level, it's evident that, for the coastal gauges, meteorological forces play a dominant role. They contribute at least 95% to the peak water level across these five gauges. Note that, as we have shown, the results for coastal gauges are not sensitive to grid resolution when the subgrid model is applied; thus, the meteorological forces play a dominant role for all grid resolutions.

Upon close inspection of Station 2 (see Figure 5), it becomes evident that the standard solution fails to accurately capture the water surface elevation. When employing the subgrid model with the same grid resolution, the root-mean-square error (E_{RMS}) value is nearly one order of magnitude smaller than the standard solution (see Table 1). This significant improvement is highlighted by plotting the maximum water surface elevation for the small area near St. Petersburg, Tampa Bay, FL, where Station 2 is located (see Figure 6). The figure illustrates that, with the coarse resolution used, the subgrid model successfully allows the water to reach Station 2, as it resolves small features in the coastline that are much smaller than the grid size. Conversely, the water surface elevation in the standard solution fails to reach this location during the flood event (Note that if the total water depth was less than 0.05 m, it is disregarded on the plot). A closer examination of the north part of Station 2 in this figure showcases the subgrid model's capacity to accurately capture the effects of narrow rivers and channels, as well as small features. This capability is lacking in the standard solution counterpart.



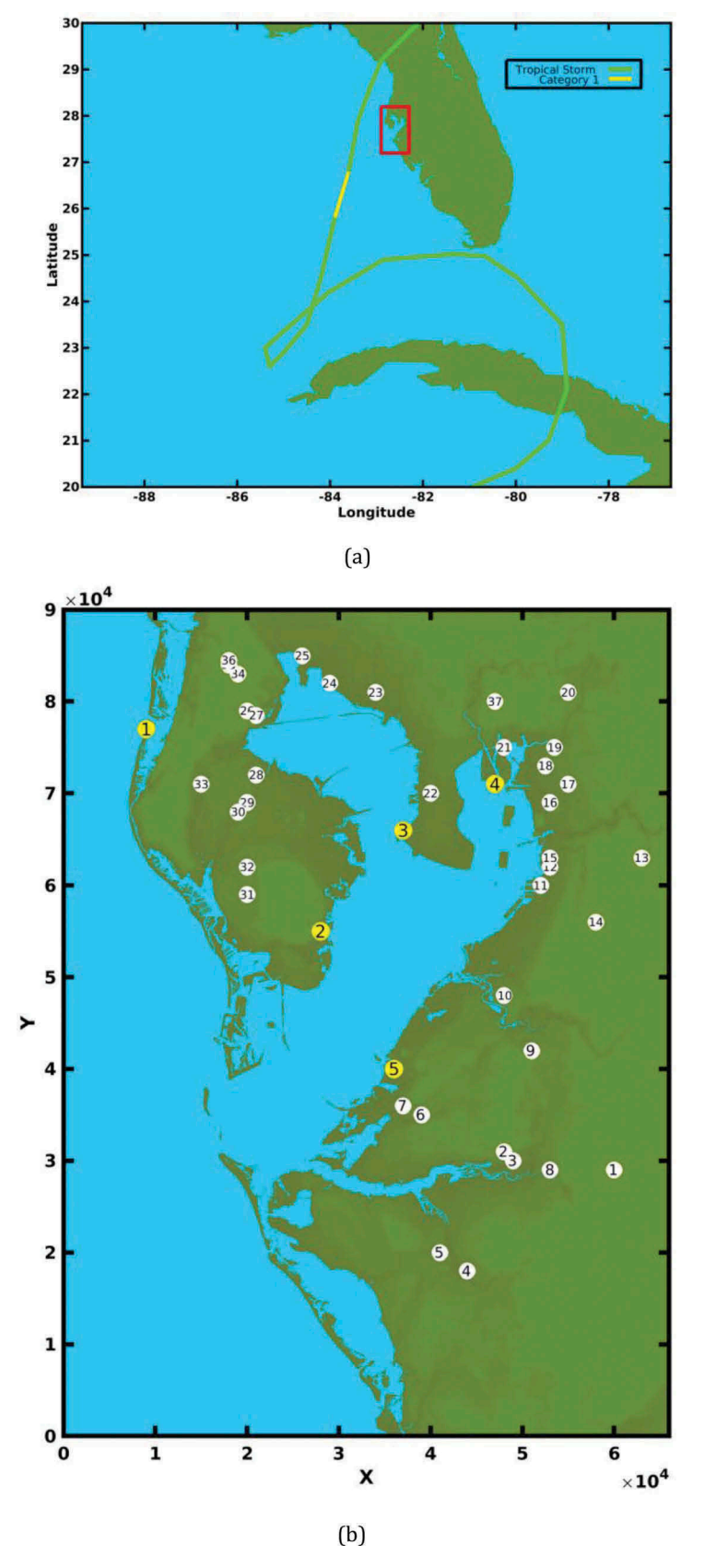


Figure 2. a) track for eta near the Florida coast, with intensities on the Saffir-Simpson scale for hurricane category 1 (H1) and tropical storm (TS), and with locations at 6-hr intervals. b) locations of USGS observations: (white circles) 37 water level sensors; and NOAA observation (yellow circles) 5 stations. The stations are described in Tables A1 and A2. The domain is in UTM zone 17N.

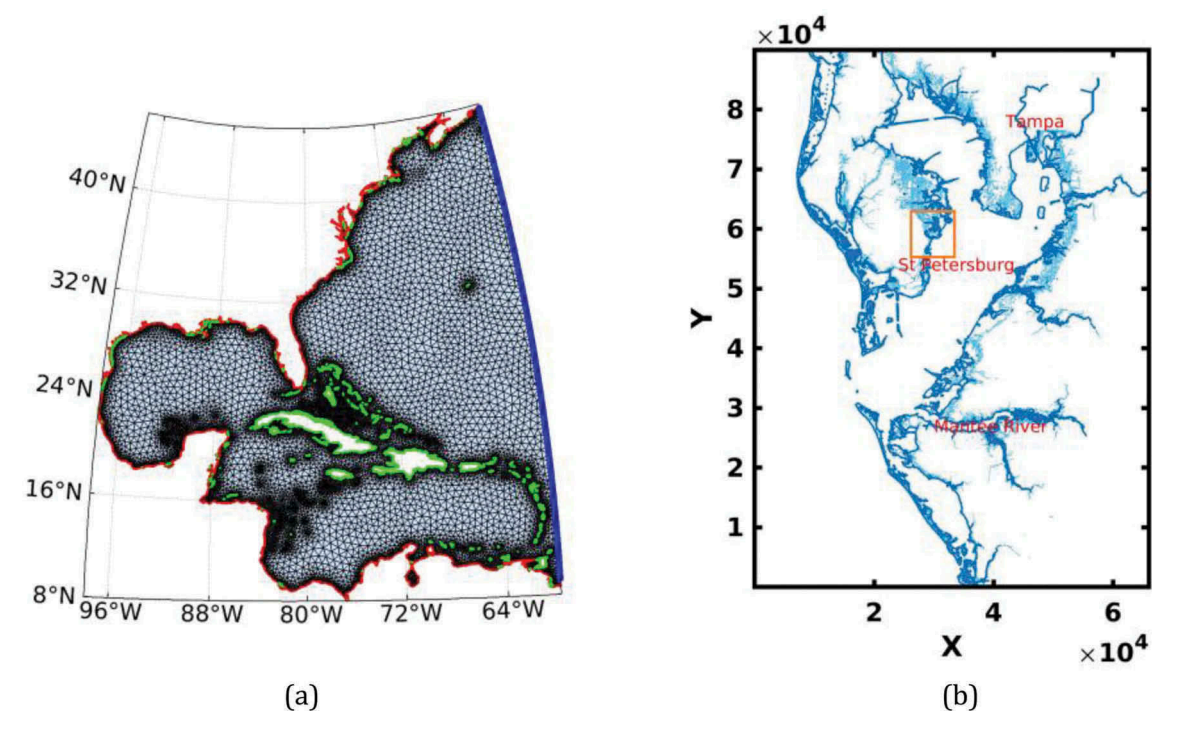


Figure 3. a) ADCIRC grid that covers the western north Atlantic Ocean, Caribbean Sea, and Gulf of Mexico. Blue line shows the open ocean boundary nodes. Red lines represent the land boundary condition. Green lines are the land boundary conditions for islands. b) CoaSToRM computational domain for Tampa bay, FL. The bathymetric data are shown with two selected contours of bathymetric depth (contour lines: 0 m; 2 m). The domain consists of 30,000 × 22000 pixels, which is used to calculate pre-storage lookup tables (the cell volume and wet area as a function of surface elevations). The CoaSToRM domain covers a rectangle with corners (82.21°W, 27.27°N) and (82.88°W, 28.08°N). The average total depth for the CoaSToRM boundary conditions is 15 m. Orange box shows the domain for Figure 6.

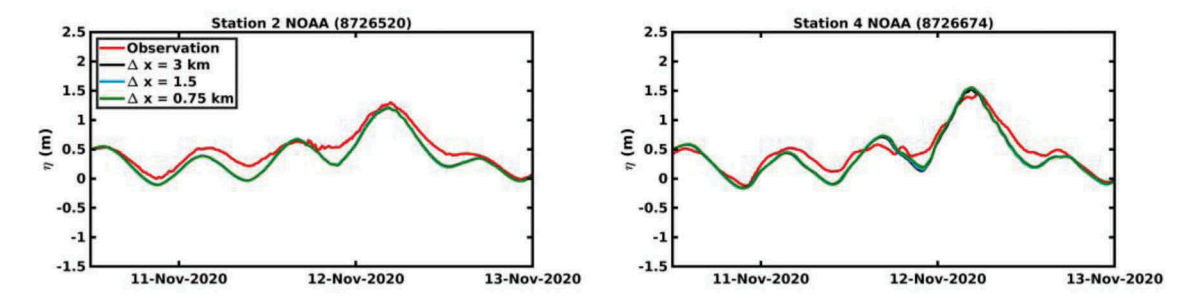


Figure 4. Time series of water surface elevation for four selected NOAA gauges with $\Delta x = 3,1.5,0.75$ km.

Table 1. Errors E_{RMS} relative to the observation (m), computed over 60 hours with 6-min sampling intervals. SG represents subgrid Model and SS shows standard solution.

Station ID (number)		8726724 (1)	8726520 (2)	8726607 (3)	8726674 (4)	8726384 (5)
Grid Resolution (km)	Configuration					
$\Delta x = 3 \text{ BC}$	SG	0.1415	0.1849	0.1892	0.1946	0.1059
$\Delta x = 3 \text{ BC} + \text{Meteo}$	SG	0.1366	0.1582	0.1404	0.1309	0.0695
$\Delta x = 3$ All forces	SS	0.1419	1.4180	0.1189	0.1181	0.0594
$\Delta x = 3$ All forces	SG	0.1298	0.1326	0.1125	0.1121	0.0584
$\Delta x = 1.5$ All forces	SG	0.1292	0.1327	0.1122	0.1004	0.0577
$\Delta x = 0.75$ All forces	SG	0.1284	0.1326	0.1135	0.0935	0.0544

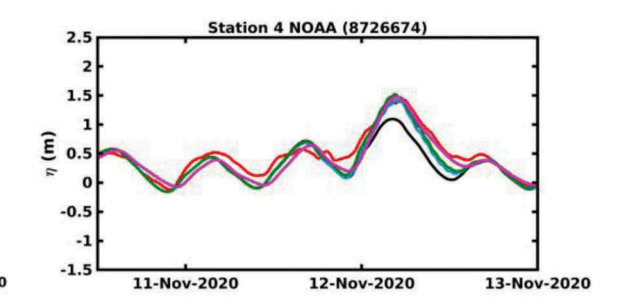


Figure 5. Time series of water surface elevations at two selected NOAA gauges ($\Delta x = 3km$).

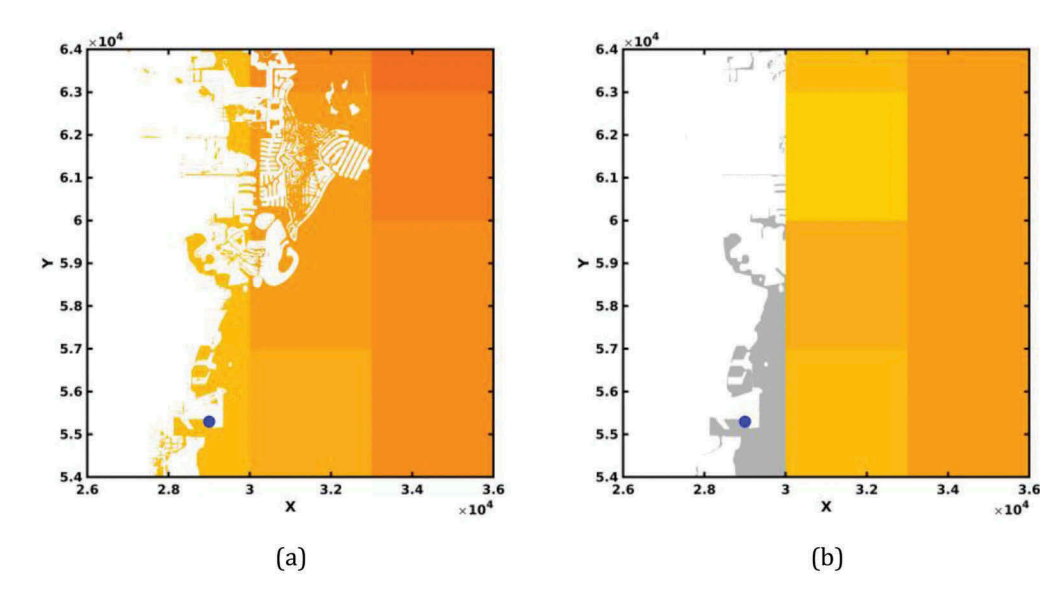


Figure 6. a) high water surface elevation for subgrid model ($\Delta x = 3$ km). b) high water surface elevation for standard solution ($\Delta x = 3$ km). The location of station 2 is shown with blue circle. The total water height less than 0.05 m is not plotted.

3.4. Predictions of inland water levels

630

640

The model predictions were evaluated at the USGS water-level sensors, where the sensors are placed far inland and near narrow rivers and features that are much smaller than the grid sizes ($\Delta x = 3 \text{ km}$, $\Delta x = 1.5 \text{ km}$, $\Delta x = 0.75 \text{ km}$). We considered three grid resolutions with all forces, including tidal and surge boundaries, river discharges, wind and pressure fields, precipitation, and infiltration. For each grid resolution, we performed two types of simulations. In the first simulation, the model was run with the cell-averaged bathymetric elevation (standard solution). In the second simulation, we applied subgrid corrections to the model.

Overall there are 37 USGS gauges in the computational domain. We selected four USGS water-level sensors scattered around Tampa Bay to demonstrate the model's performance in the region. These stations are in proximity to the Manatee River (Station 8), Alafia River (Station 17), Palm River (Station 19), and the middle of Cross Bayou Canal (Station 29). As shown in Figure 7, for all selected locations, the standard solutions with different resolutions show a roughly constant surface elevation. The reason is the inability of

the standard solution to capture the effects of rivers, channels and features that are much smaller than the grid cell. However, the subgrid model outperforms the standard solutions in these locations. Overall, at locations farther inland, the flooding event could only be predicted with the subgrid model, due to its ability to represent flow pathways below the model scale.

0.5

660

675

Upon close inspection of Figure 7, for Stations 17 and 29, located in the northeast and northwest of Tampa Bay (see Figure 2), respectively, increasing the resolution improves the accuracy of the subgrid model. The higher resolution model provides more accurate results compared to the observations. On the other hand, Station 8, situated in the east side of Tampa Bay at Manatee River in Rye, FL, shows nearly identical water surface elevations for all grids with subgrid corrections. At Station 19, the coarsest grid underestimates the water surface elevation, while higher resolutions overestimate it. Generally, the performance of the subgrid model tends to vary spatially across different resolutions. However, increasing the resolution results in a slight increase in accuracy, which is a consequence of representing the computational domain with more degrees of freedom.

72.0

725

730

735

740

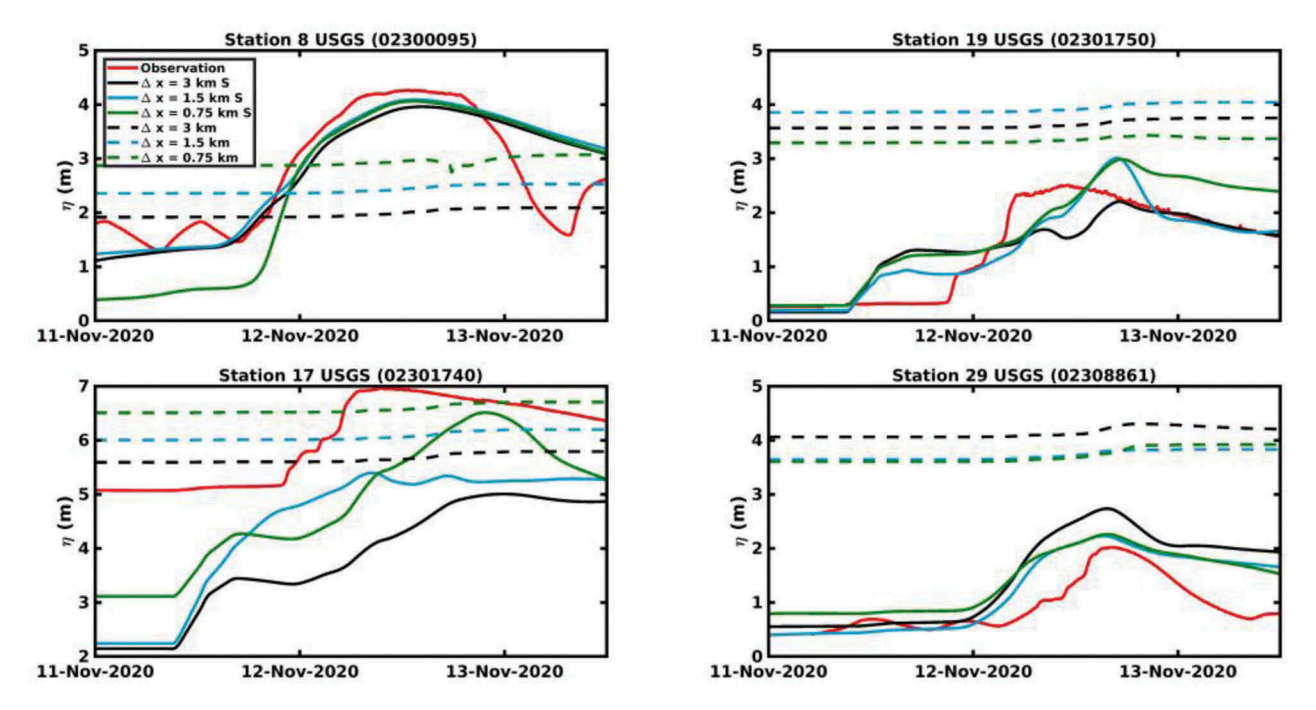


Figure 7. Time series of water surface elevation for four selected USGS gauges.

By careful examination of the timing of peak flooding for all these stations, it is evident that the peak of inland flooding occurs between 16:00 and 22:00 on November 12th. In contrast, the peak of coastal flooding happens around 4:00 to 6:00 on November 12th. This discrepancy highlights the delay in flooding attributed to pluvial and fluvial processes.

680

690

695

700

705

To better understand the impact of various drivers, we applied subgrid methods at a grid resolution of Δx = 3 km in three distinct simulations. The first simulation used ADCIRC boundary conditions and meteorological forces; the second simulation added spatially varying rainfall and infiltration, and the third simulation added river discharges. This sequential approach allowed for a comprehensive exploration of the interplay between various forces influencing the system under study. Figure 8 displays the time series of surface elevation for the three simulations and observed water surface elevation for four selected USGS gauges. Additionally, the local rainfall for each location is plotted on the right y-axis. For stations 8, 17, and 19, the impact of incorporating rainfall and river discharges on the simulation results is evident. These stations are situated near rivers and channels, making them susceptible to the influence of river discharges. Conversely, station 29 is primarily affected by local rainfall alone. Located far from rivers, channels, and disconnected from the bay, station 29 is predominantly influenced by local rainfall patterns. The findings indicate that without accounting for pluvial and fluvial factors (rainfall, infiltration, and river discharges), there is no significant inland flooding in the region. This suggests that inland flooding is primarily influenced by hydrological drivers. Note that the results consistently follow the same trend across all grid resolutions when the subgrid model is applied.

Comparing the time series of surface elevations for coastal flood gauges with those for inland flood gauges (see Figures 4 and 7), it can be observed that the time series of surface elevation for the coastal gauges (Figure 4) are less sensitive to changes in grid resolution compared to the inland gauges (Figure 7). This issue mainly arises because the runoff process cannot be capture at the scale smaller the computational grid. However, these errors diminish as finer resolutions are employed. whenever rainfall contributes significantly to the peak surface elevation, grid dependency becomes a more significant concern. For example, at Stations 17, 19, and 29, rainfall contributes to more than 60% of the peak water surface elevation, resulting in evident grid dependency. Conversely, at Station 8, water discharge has a larger impact on the peak surface elevation, resulting in nearly identical surface elevations across all grid sizes, similar to the coastal gauges.

3.5. Predictions of peak water levels

The high water mark (HWM) refers to the highest level the water can reach during a flood event. Eta's effects on water levels in Tampa Bay are described at the selected stations in the previous sections, but here more comprehensively at the 37 USGS stations and 5 NOAA tide and currents gauges. Combining observed peak water levels from the sensors allows the creation of a more extensive inundation dataset. Then, the models' performance can be quantified through

755

765

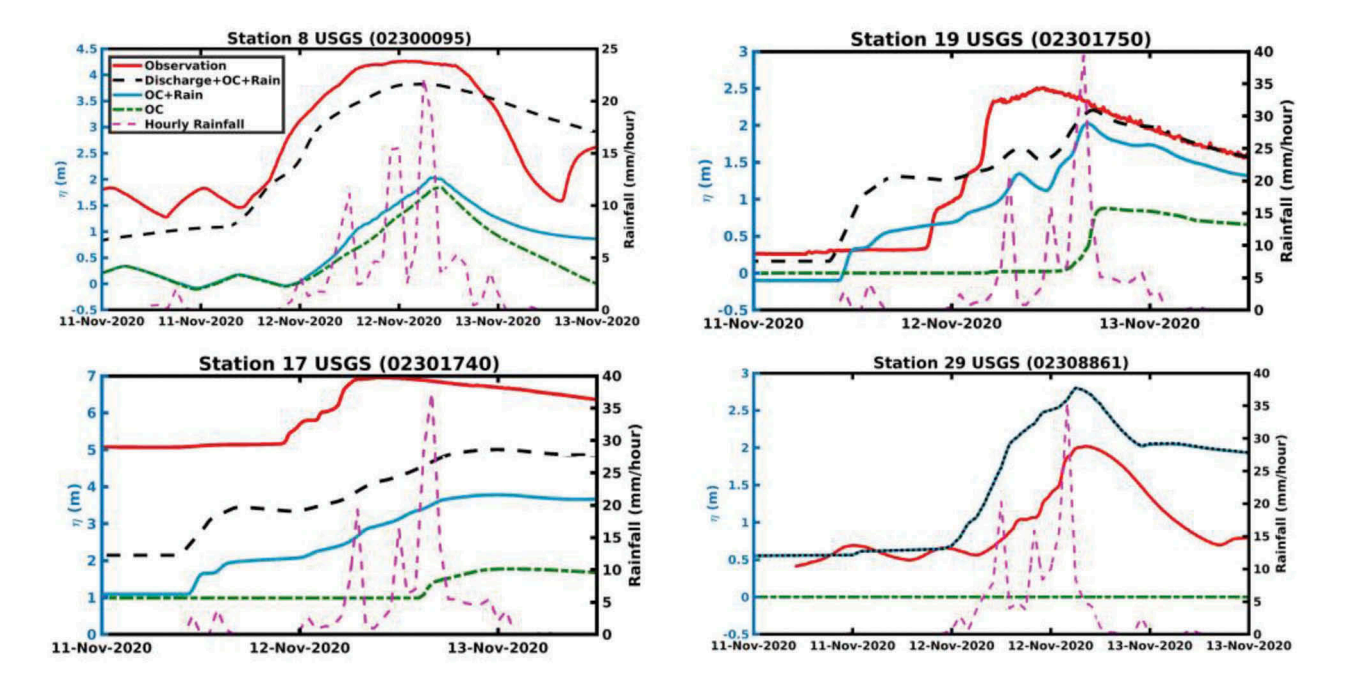


Figure 8. Time series of water surface elevation for four selected USGS gauges. 'OC' represents the first simulation, which includes ADCIRC boundary conditions and meteorological forces. 'OC+Rain' denotes the second simulation, where spatially varying rainfall and infiltration are incorporated into the model. 'Discharge+OC+Rain' indicates the simulation where river discharges are considered in addition to the conditions in simulation 2.

a comparison of peak to peak values between observations and predictions.

Three quantities are used to measure the model performance for each simulation: (1) Root-meansquare error (RMSE) is used as a measure of the magnitude of error (and is calculated based on peak water levels for all stations); (2) best-fit slope (a from y = axline), which describes how well a regression line fits a dataset, and (3) coefficient of determination (R^2) , which indicates the overall performance of the model to predict the magnitude of the peak surge, this is calculated relative to the 1:1 line. The optimal agreement for each of these metrics corresponds to RMSE = 0, $R^2 = 1$, and a = 1.

Figure 9 demonstrates the correlation between observed and modeled HWMs, showing a slope close to unity for the subgrid models. In contrast, the slopes for standard solution counterparts are larger than unity. For the standard solution on either grid, the R^2 values are much smaller than those of the subgrid model. Examining standard solutions reveals that increasing the resolutions lead to enhanced model accuracy, with R^2 values increasing and RMSE decreasing significantly. Comparing the subgrid model with different resolutions, it is noticeable that the R^2 values improve slightly with increasing the resolution, suggesting a better match with a discernible scatter. However, it is worth noting that these error statistics could be further improved with higher-resolution grids, fully dynamic atmospheric forcing, inclusion of wind waves, among other factors.

The blue line (—) is the best fit (y = ax) for subgrid model. The red line (----) denotes the best fit (y = ax)for standard solution.

Figure 10 provides an overview of the maximum water depths experienced in Pinellas County during Hurricane Eta. The results show that the patterns of water lever peaks are quite similar across all grid resolutions. Despite the similarity in result patterns, it is apparent that the higher resolution results depict a low-depth flood in the middle of the domain that is absent in the coarser resolution. This disparity primarily arises from the inability of the coarser grid to capture small-scale runoff processes, pointing out these small differences. In Tampa Bay, flood depths range from 1 to 2.5 m near the bay, decreasing as we move farther inland. As expected, flooding is less severe farther away from the bay.

780

785

790

795

800

3.6. Computational cost

The subgrid model introduced here does come with an extra computational cost for each simulation. However, we tried to minimize this extra cost via certain improvements to the model to reduce the computational burden. One such improvement is the incorporation of lookup tables, which effectively lowers the model's computational requirements. A prestorage lookup table is implemented to store the volume and the wet area of the cells as a function of surface elevations. Lookup tables can be built once and for all cells as a pre-processing step. This implementation is seamlessly integrated into the code,

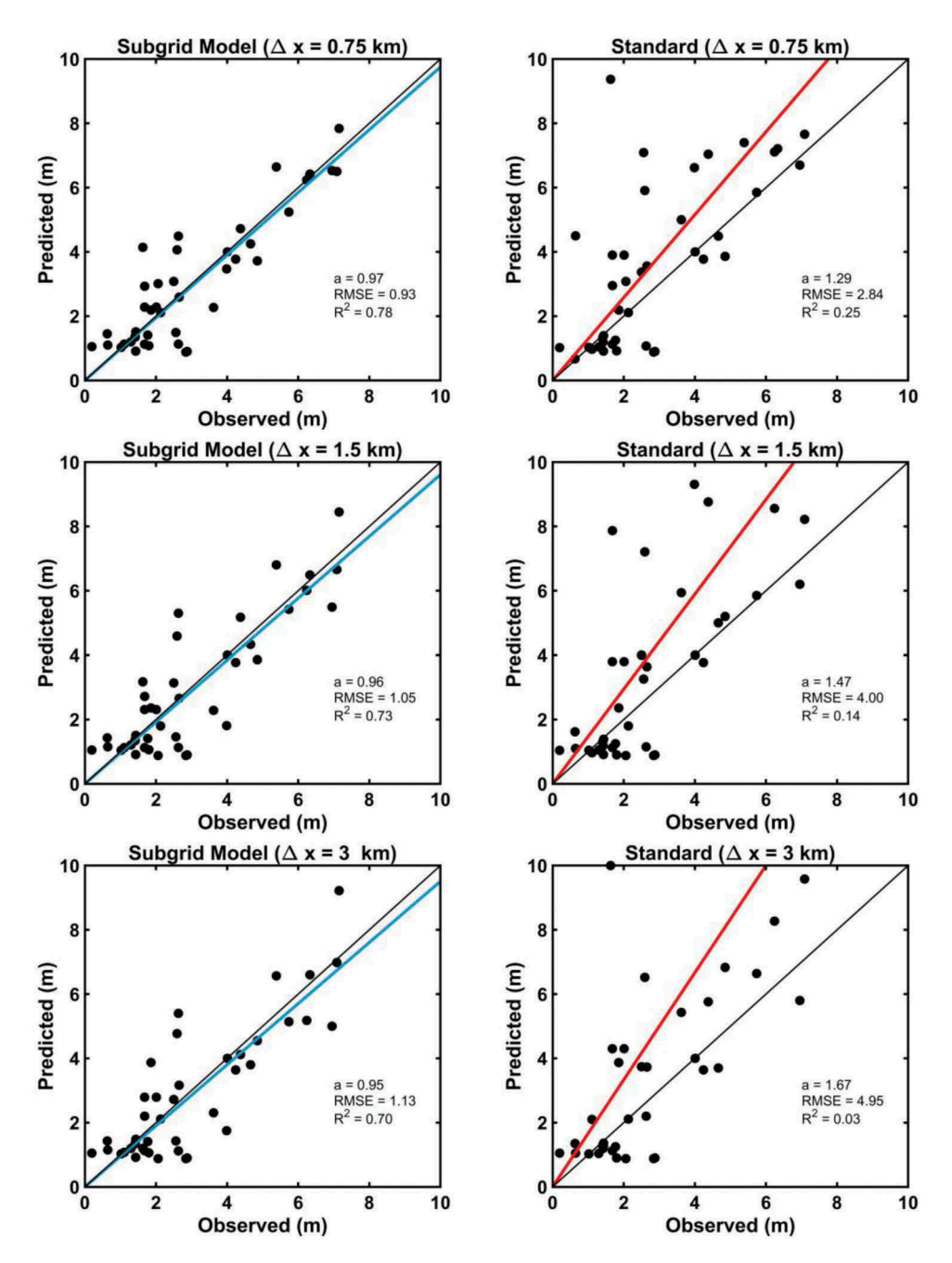


Figure 9. Comparison of observed and predicted peak waterlevels for Eta2020.Eta2020.The solid black circles(•). are the peak of the water levels predicted by each model's resolution.Resolution.The black solid line(—) is 1:1 line.

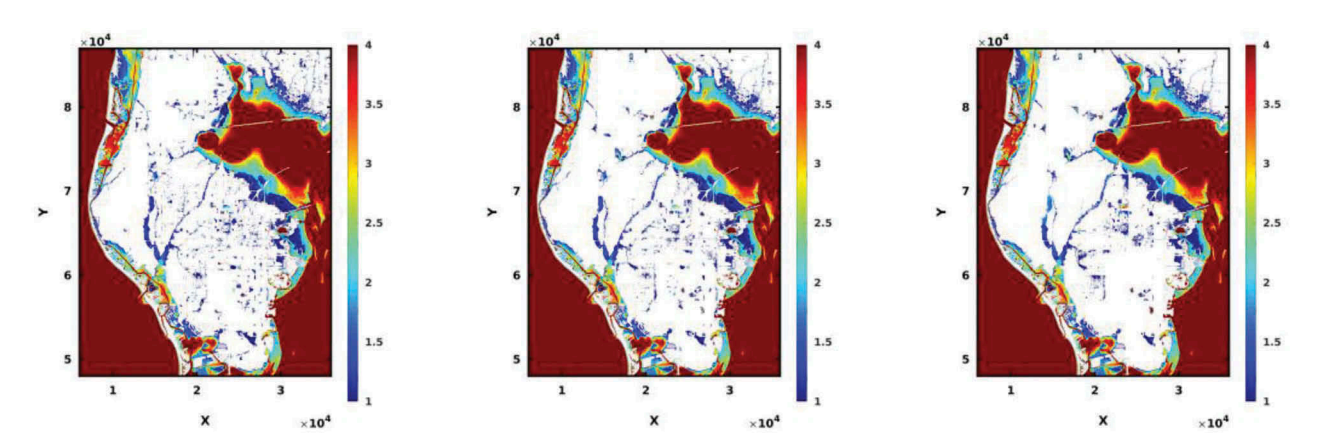


Figure 10. Modeled maximum water depths in Pinellas County during hurricane eta for water depths greater than 0.5 m. From left to right, the panels show $\Delta x = 0.75$ km, $\Delta x = 1.5$ km, and $\Delta x = 3$ km. All subgrid results are downscaled based on high-resolution bathymetry data (3 m resolution).

810

815

825

830

835

840

845

Table 2. The table presents computational costs, with all times expressed in decimal minutes.

Grid size (km)	$\Delta x = 3$	$\Delta x = 1.5$	$\Delta x = 0.75$
Subgrid model with lookup table	0.0695	0.2292	3.7211
Standard solution	0.0231	0.1933	3.6905
Lookuptable computational cost	0.0389	0.0358	0.0306
Subgrid model without lookup table	12.0414	29.9361	68.1331

making it more user-friendly. Note that implementing the lookup table within the code does add computational cost, but it provides the advantage of enabling CoaSToRM to run on any grid resolution effortlessly. This flexibility in handling various grid resolutions is a significant benefit of the model.

Table 2 displays the reported computational costs (walltime duration) for both the subgrid and the standard models. We also show the computational cost when the lookup table is not utilized, along with the additional time taken by the code to generate the lookup table. Note that without lookup tables, the model must compute all integrals in the subgrid levels numerically, leading to computational expense. Firstly, it is apparent that without the use of the lookup table, the computational cost increases significantly. Additionally, the introduction of the subgrid model with lookup table results in a marginal rise in the computational cost. However, this enhancement significantly improves the accuracy of the results. For instance, with the coarsest grid ($\Delta x = 3km$), the R^2 value was approximately 0.03. By incorporating the subgrid model, the computational time increases by a few minutes, but the R^2 value rises to 0.70, which represents a considerable improvement. Overall, comparing subgrid models with different resolutions, we find that a 3-km subgrid simulation runs roughly 50 times faster than a 0.75-km subgrid simulation while maintaining accuracy. Note that if the computational cost of building lookup tables is not taken into account, the subgrid model contributes an increase of approximately 2% to 35% in the overall computational cost. All simulations are performed on a single core with a 2.8 GHz Intel CPU.

In general, while subgrid corrections add extra computational cost to the model, the subgrid results on coarser grids demonstrate greater accuracy compared to standard

solutions. As a result, for achieving a desired level of accuracy (e.g. an acceptable *RMSE* value), the subgrid model can be applied on a coarser grid, leading to faster computations. Consequently, considering both accuracy and computational cost, the subgrid model offers a significant gain in computational efficiency.

4. Discussion and conclusions

In this study, a subgrid method was employed for compound flood modeling, aiming to enhance flood prediction while performing on a relatively coarse grid resolution, which offers considerable computational efficiency. Here, we adopt the model presented by Kennedy et al. (2019) but with additions for spatially-varying precipitation, infiltration, friction, atmospheric pressure, and wind stress. The final governing equations are discretized with a semi-implicit finite-difference method on a staggered C-grid (Arakawa and Lamb 1977).

855

875

880

885

890

895

900

905

Several key considerations emerge from our $\,860$ findings.

- (1) First, decisions about grid resolution are essential. Increasing the resolution can reduce the computational cost while maintaining accuracy, but the grid size must provide the model with the ability to represent the real dynamics of the problem with a sufficient degree of freedom. For instance, we have assumed that each computational cell (coarse cell) has a single surface elevation (one degree of freedom), which is equal to the average surface elevation within the coarse cell area. If the variation of surface elevation within the coarse cell is not large, then the assumption is valid. However, in practical scenarios, when employing an excessively large cell that exhibits a significant variation in surface elevation at the subgrid level, a single surface elevation cannot adequately represent the large gradient of surge elevation within that coarse cell. Consequently, the cell would require a higher degree of freedom for the surface elevation (using more than one surface elevation to represent the cell surface elevation) to accurately represent this. The choice of the coarse grid is mainly based on the application context.
- (2) Second, drawing from previous subgrid modeling experiences, challenges related to the representation of flow between hydraulically disconnected regions were noted by Casulli (2019). Although solutions such as incorporating cell clones have been proposed by Begmohammadi et al. (2021), this study uses a blocking solution for simplicity and practicality. The framework has the potential to update with more complex methodology in the future.
- (3) Third, a temporally constant, spatially varying infiltration method is employed in the model. This method offers several advantages, including a more realistic representation of infiltration patterns across the study area compared to uniform infiltration rates. However, it is essential to acknowledge that this method still simplifies complex hydrological processes and may not fully account for all influencing factors. In the future, we plan to enhance the model by implementing more sophisticated infiltration methods that consider additional variables such as soil

970

975

980

985

990

1000

1005

Q4

- characteristics, land cover types, and rainfall intensity, aiming to further improve the accuracy and reliability of the model's predictions.
- (4) Fourth, it is important to note that aspects such as stormwater drainage and wave effects were not included in the current model. However, there is potential for future versions of the model to incorporate these effects.

910

915

920

925

930

935

940

945

950

955

960

(5) Fifth, the model is written in a single core and it is appropriate to be used for the coarse resolution simulations with the subgrid approach. We plan to include MPI or OpenMP in future versions to enhance parallel processing capabilities. Note that for the example presented herein, it is feasible to execute the model at resolutions finer than 750 m, contingent upon the availability of suitable hardware.

While acknowledging inherent limitations, the methodology presented serves as a foundational framework for compound flooding simulation, with ongoing efforts aimed at continuous improvement to address practical considerations and advancements in the field.

Finally, the model performance is evaluated for Hurricane Eta 2020 in Tampa Bay, FL. Here are the major findings:

- (1) Various types of forcing are important in compound flooding. We demonstrated that a comprehensive model, which simultaneously considers surge and tidal boundary conditions, meteorological forces, precipitation, infiltration, and spatially-varying friction, is essential for studying compound flooding along coastlines. We showed that incorporating meteorological forces, precipitation, and infiltration on the top of tidal boundary conditions improves the peak surge prediction at four NOAA gauges along the coastline. Overall, at coastal locations, the hydrodynamic forces are the primary drivers to the peak water levels but hydrologic forces can contribute as much as 5% of the peak water levels. Conversely at inland locations, the hydrologic forces become important, and they contribute over 85% to the peak water levels.
- (2) Subgrid corrections improve the accuracy of the model by resolving features that are much smaller than the grid scale. We showed that the utilization of the subgrid model better captures the effects of narrow channels and small features along the coastlines compared to the standard solution at the same grid resolution. The performance of the subgrid model was evaluated in real scenarios, such as the inundation caused by Hurricane Eta. The subgrid model exhibits improvements across all statistical measures, encompassing the RMSE error, the R^2 value, and the slope of the linear best fit, which are

used to assess the model's predictive capacity for the peak water levels at various locations. For the grid sizes investigated in this study (3 to 0.75-km), the subgrid model enhances the R^2 and RMSE values from approximately 0.03 to 0.25 and 4.95 to 2.84, as seen in the standard solutions, to around 0.70 to 0.78 and 1.13 to 0.93 for the subgrid model, respectively.

(3) For a given grid configuration, integrating subgrid corrections leads to a moderate increase in computational expenses. In our current implementation, the incorporation of the subgrid model raises the computational cost by 2% to 35%

on the same grid when the lookup table is employed externally to the model. Although introducing lookup tables does come with an associated computational cost, it substantially enhances the convenience of using the code. Therefore, the additional computational expenses are minor when weighed against the accuracy gains achieved by applying subgrid corrections to coarser grids. Furthermore, we have demonstrated the necessity of utilizing lookup tables, as the subgrid model without them results in a substantial computational expense. In addition, the semi-implicit discretization used here allows for larger time steps, which can lead to significant computational efficiency gains. It reduces the computational burden and makes simulations faster, enabling the study of larger and more intricate domains (Casulli 1990).

These findings have implications for coastal flood forecasting, where a large number of ensemble forecasting may be run in a short time and risk assessment, where thousands of realizations may be required, as the proposed model offers higher accuracy (via better representation of small-scale flow pathways and barriers) and/or higher efficiency (via faster run-times by using coarsened grids).

Disclosure statement

No potential conflict of interest was reported by the author(s).

Funding

We appreciate the funding provided by the National Science Foundation under Award Number 2103754, which significantly supported this research. The study also benefited from the support of National Science Foundation grants ICER 1664037 and 1664040. We thank the National Science Foundation for their crucial contributions to this project.

Data availability statement

CoaSToRM is shared freely with academic researchers 1010 (https://github.com/ab3838/CoaSToRM).

1020

1025

1030

1035

1045

1050

1055

1060

1065

1070

1075

Q5

References

Amirhosein, Begmohammadi, Damrongsak Wirasaet, Zachariah Silver, Diogo Bolster, Andrew B Kennedy, and J. C. Dietrich. 2021. "Subgrid Surface Connectivity for Storm Surge Modeling." Advances in Water Resources https://doi.org/10.1016/j.advwatres.2021.

Arakawa, Akio, and Vivian R Lamb. 1977. "Computational Design of the Basic Dynamical Processes of the UCLA General Circulation Model." General Circulation Models of the Atmosphere 17 (Supplement C): 173-265.

Bates, Paul D, and A. P. J. De Roo. 2000. "A Simple Raster-Based Model for Flood Inundation Simulation." Journal of Hydrology 236 (1-2): 54-77. https://doi.org/10. 1016/S0022-1694(00)00278-X.

Bates, Paul D, Niall Quinn, Christopher Sampson, Andrew Smith, Oliver Wing, Jeison Sosa, James Savage, et al. 2021. "Combined Modeling of US Fluvial, Pluvial, and Coastal Flood Hazard Under Current and Future Climates." Water Resources Research 57 (2): e2020WR028673. https:// doi.org/10.1029/2020WR028673.

Begmohammadi, Amirhosein, Damrongsak Wirasaet, Autumn Poisson, Johnathan L Woodruff, J. Casey Dietrich, Diogo Bolster, and Andrew B Kennedy. 2023. "Numerical Extensions to Incorporate Subgrid Corrections in an Established Storm Surge Model." Coastal Engineering Journal 65 (2): 175-197. https://doi. org/10.1080/21664250.2022.2159290.

1040 Bilskie, M. V., and S. C. Hagen. 2018. "Defining Flood Zone Transitions in Low-Gradient Coastal Regions." Geophysical Research Letters 45 (6): 2761-2770. https://doi.org/10. 1002/2018GL077524.

> Brunner, Gary W. 2016. "HEC-RAS River Analysis System: Hydraulic Reference Manual, Version 5.0." US Army Corps of Engineers-Hydrologic Engineering Center 547.

> Canestrelli, Alberto, and Eleuterio F Toro. 2012. "Restoration of the Contact Surface in FORCE-Type Centred Schemes II: Non-Conservative One-And Two-Layer Two-Dimensional Shallow Water Equations." Advances in Water Resources 47:76-87. https://doi.org/10.1016/j.advwatres.2012.03.018.

> Casulli, Vincenzo. 1990. "Semi-Implicit Finite Difference Methods for the Two-Dimensional Shallow Water Equations." Journal of Computational Physics 86 (1): 56-74. https://doi.org/10.1016/0021-9991(90)90091-E.

> Casulli, Vincenzo. 2009. "A High-Resolution Wetting and Drying Algorithm for Free-Surface Hydrodynamics." International Journal for Numerical Methods in Fluids 60 (4): 391-408. https://doi.org/10.1002/fld.1896.

Casulli, Vincenzo. 2019. "Computational Grid, Subgrid, and Pixels." International Journal for Numerical Methods in Fluids 90 (3): 140-155. https://doi.org/10.1002/fld.4715.

Casulli, Vincenzo, and Guus S Stelling. 2011. "Semi-Implicit Subgrid Modelling of Three dimensional Free-Surface Flows." International Journal for Numerical Methods in Fluids 67 (4): 441-449. https://doi.org/10.1002/fld.2361.

Chen, Changsheng, Robert C Beardsley, Joannes J Westerink Richard A Luettich Jr, Harry Wang, Will Perrie, Qichun Xu, Q. Xu, et al. 2013. "Extratropical Storm Inundation Testbed: Intermodel Comparisons in Scituate, Massachusetts." Journal of Geophysical Research Oceans 118 (10): 5054–5073. https://doi.org/10.1002/jgrc.20397.

Cho, Kyoung-Ho, Harry V Wang, Jian Shen, Arnoldo Valle-Levinson, and Yi-cheng Teng. 2012. "A Modeling Study on the Response of Chesapeake Bay to Hurricane Events of Floyd and Isabel." Ocean Modelling 49:22-46. https:// doi.org/10.1016/j.ocemod.2012.02.005.

CIRES (Cooperative Institute for Research in Environmental Sciences). 2014. Continuously Updated Digital Elevation Model (CUDEM)—1/9 Arc-Second Resolution Bathymetric topographic Tiles.

Defina, Andrea. 2000. "Two-Dimensional Shallow Flow Equations for Partially Dry Areas." Water Resources Research 36 (11): 3251-3264. https://doi.org/10.1029/ 2000WR900167.

Dietrich, J. C., M. Zijlema, J. J. Westerink, L. H. Holthuijsen, C. Dawson, RE Jensen Ra Luettich Jr, J. M. Smith, G. S. Stelling, and G. W. Stone. 2011. "Modeling Hurricane Waves and Storm Surge Using Integrally-Coupled, Scalable Computations." Coastal Engineering 58 (1): 45–65. https://doi.org/10.1016/j.coastaleng.2010.08.001.

Dresback, Kendra M, Jason G Fleming, Brian O Blanton, Carola Kaiser, Jonathan J Gourley, Evan M Tromble, Richard A Luettich Jr, et al. 2013. "Skill Assessment of a Real-Time Forecast System Utilizing a Coupled Hydrologic and Coastal Hydrodynamic Model During Hurricane Irene (2011)." Continental Shelf Research 71:78-94. https://doi. org/10.1016/j.csr.2013.10.007.

Dresback, Kendra M, Randall L Kolar, and J. Casey Dietrich. 2005. "On the Form of the Momentum Equation for Shallow Water Models Based on the Generalized Wave Continuity Equation." Advances in Water Resources 28 (4): 345-358. https://doi.org/10.1016/j.advwatres.2004.11.011.

Du, J. 2011. "NCEP/EMC 4KM Gridded Data (GRIB) Stage IV Data."

Egbert, Gary D, and Svetlana Y Erofeeva. 2002. "Efficient Inverse Modeling of Barotropic Ocean Tides." Journal of Atmospheric and Oceanic Technology 19 (2): 183-204. https://doi.org/10.1175/1520-0426(2002)019<0183: EIMOBO>2.0.CO;2.

Garratt, J. R. 1977. "Review of Drag Coefficients Over Oceans and Continents." Monthly Weather Review 105 (7): https://doi.org/10.1175/1520-0493(1977) 105<0915:RODCOO>2.0.CO;2.

Gori, Avantika, Ning Lin, and James Smith. 2020. "Assessing Compound Flooding from Landfalling Tropical Cyclones on the North Carolina Coast." Water Resources Research (4): e2019WR026788. https://doi.org/10.1029/ 56 2019WR026788.

Hodges, Ben R. 2015. "Representing Hydrodynamically Important Blocking Features in Coastal or Riverine Lidar Topography." Natural Hazards and Earth System Sciences 15 (5): 1011-1023. https://doi.org/10.5194/nhess-15-1011-2015.

Holland, Greg J. 1982. Tropical Cyclone Motion: Environmental Interaction Plus a Beta Effect. Department of Atmospheric Science, Colorado State University.

Jelesnianski, Chester P. 1992. SLOSH: Sea, Lake, and Overland Surges from Hurricanes. Vol. 48. US Department of Commerce, National Oceanic and Atmospheric Administration

Jin, Teng, Anthony J Jakeman, Jai Vaze, Barry FW Croke, Dushmanta Dutta, and S. J. E. M. Kim. 2017. "Flood Inundation Modelling: A Review of Methods, Recent Advances and Uncertainty Analysis." Environmental Modelling & Software 90:201-216. https://doi.org/10. 1016/j.envsoft.2017.01.006.

Kennedy, Andrew В. Damrongsak Wirasaet. Amirhosein Begmohammadi, Thomas Sherman, Diogo Bolster, and J. C. Dietrich. 2019. "Subgrid Theory for Storm Surge Modeling." Ocean Modelling 144:101491. https://doi.org/10.1016/j.ocemod.2019.101491.

Kerr, P. C., A. S. Donahue, Joannes J Westerink, LY Zheng Ra Luettich Jr, Robert H Weisberg, Y. Huang, Y. Huang, et al. 1080 Q13

1085

1090

1100

1105

Q6

1110

1115

1120

Q7

1130

Q8

1135

1140

		COASTAL ENGINEERING JOURNAL 🥌 17	
1145	2013. "US IOOS Coastal and Ocean Modeling Testbed: Inter-Model Evaluation of Tides, Waves, and Hurricane Surge in the Gulf of Mexico." <i>Journal of Geophysical Research Oceans</i> 118 (10): 5129–5172. https://doi.org/10.1002/jgrc.20376.	Watersheds." Environmental Modelling & Software 119:166–181. https://doi.org/10.1016/j.envsoft.2019.06.002. Sarhadi, Ali, Rapha¨el Rousseau-Rizzi, Mandli Kyle, Neal Jeffrey, P Wiper Michael, Feldmann Monika, and Emanuel. Kerry. 2024. "Climate Change Contributions to	1215
1150	Leijnse, Tim, Maarten van Ormondt, Kees Nederhoff, and Ap van Dongeren. 2021. "Modeling Compound Flooding in Coastal Systems Using a Computationally Efficient	Increasing Compound Flooding Risk in New York City." Bulletin of the American Meteorological Society 105 (2): E337–E356. https://doi.org/10.1175/BAMS-D-23-0177.1.	1220
1155	Reduced-Physics Solver: Including Fluvial, Pluvial, Tidal, Wind-And Wave-Driven Processes." <i>Coastal Engineering</i> 163:103796. https://doi.org/10.1016/j.coastaleng.2020.	U.S. Geological Survey. n.d. "USGS Water Data Mapper." Accessed June 11, 2024. https://maps.waterdata.usgs.gov/mapper/index.html.	1220
1160	103796. Li, Z., and Ben R Hodges. 2019. "Model Instability and Channel Connectivity for 2D Coastal Marsh Simulations." <i>Environmental Fluid Mechanics</i> 19 (5): 1309–1338. https://doi.org/10.1007/s10652-018-9623-7.	Volp, N. D., B. C. Van Prooijen, and G. S. Stelling. 2013. "A Finite Volume Approach for Shallow Water Flow Accounting for High-Resolution Bathymetry and Roughness Data." <i>Water Resources Research</i> 49 (7): 4126–4135. https://doi.org/10.1002/wrcr.20324.	1225
	Lin, Ning, and Kerry Emanuel. 2016. "Grey Swan Tropical Cyclones." <i>Nature Climate Change</i> 6 (1): 106–111. https://doi.org/10.1038/nclimate2777. Luettich, Richard Albert, Joannes J Westerink, Norman	Weisberg, Robert H, and Lianyuan Zheng. 2006. "Hurricane Storm Surge Simulations for Tampa Bay." <i>Estuaries and Coasts</i> 29 (6): 899–913. https://doi.org/10.1007/BF02798649.	1230
1165	W Scheffner, et al. 1992. ADCIRC: An Advanced Three-Dimensional Circulation Model for Shelves, Coasts, and Estuaries. Report 1, Theory and Methodology of ADCIRC-2DD1 and ADCIRC-3DL. Report.	Whitaker, Stephen. 1998. <i>The Method of Volume Averaging</i> . Vol. 13. Springer Science & Business Media. Wing, Oliver EJ, Christopher C Sampson, Paul D Bates, Niall Quinn, Andrew M Smith, and Jeffrey C Neal. 2019.	1235
1170	Mishra, Surendra Kumar, and Vijay P Singh. 1999. "Another Look at SCS-CN Method." <i>Journal of Hydrologic Engineering</i> 4 (3): 257–264. https://doi.org/10.1061/(ASCE)1084-0699 (1999)4:3(257).	"A Flood Inundation Forecast of Hurricane Harvey Using a Continental scale 2D Hydrodynamic Model." <i>Journal of Hydrology X</i> 4:100039. https://doi.org/10.1016/j.hydroa. 2019.100039.	
1175	National Oceanic and Atmospheric Administration. n.d. "NOAA Tides and Currents Water Levels." Accessed June 11, 2024. https://tidesandcurrents.noaa.gov/waterlevels. html. Neal, Jeffrey, Guy Schumann, and Paul Bates. 2012.	Woodruff, Johnathan, J. C. Dietrich, D. Wirasaet, A. B. Kennedy, and D. Bolster. 2023. "Storm Surge Predictions from Ocean to Subgrid Scales." <i>Natural Hazards</i> 117 (3): 2989–3019. https://doi.org/10.1007/s11069-023-05975-2.	1240
1180	"A Subgrid Channel Model for Simulating River Hydraulics and Floodplain Inundation Over Large and Data Sparse Areas." Water Resources Research 48 (11).	Woodruff, Johnathan L, J. C. Dietrich, D. Wirasaet, A. B. Kennedy, D. Bolster, Z. Silver, S. D. Medlin, and R. L. Kolar. 2021. "Subgrid Corrections in Finite-Element	1245
1100	https://doi.org/10.1029/2012WR012514. Nederhoff, Kees, Tim WB Leijnse, Kai Parker, Jennifer Thomas, Andrea O'Neill, Maarten van Ormondt, Robert McCall, et al.	Modeling of Storm-Driven Coastal Flooding." <i>Ocean Modelling</i> 167:101887. https://doi.org/10.1016/j.ocemod. 2021.101887.	1250
1185	2024. "Tropical or Extratropical Cyclones: What Drives the Compound Flood Hazard, Impact, and Risk for the United States Southeast Atlantic Coast?" <i>Natural Hazards</i> 1–47. https://doi.org/10.1007/s11069-024-06552-x.	Wu, Guoxiang, Fengyan Shi, James T Kirby, Ryan Mieras, Bingchen Liang, Huajun Li, and Jian Shi. 2016. "A Pre-Storage, Subgrid Model for Simulating Flooding and Draining Processes in Salt Marshes." <i>Coastal Engineering</i>	
1190	Pasch, R., B. Reinhart, R. Berg, and D. Roberts. 2021. "National Hurricane Center Tropical Cyclone Report." <i>Hurricane Eta</i> : 1–70. Platzek, F. W., G. S. Stelling, J. A. Jankowski, R. Patzwahl, and	108:65–78. https://doi.org/10.1016/j.coastaleng.2015.11.008. Yankovsky, Alexander E. 2009. "Large-Scale Edge Waves Generated by Hurricane Landfall." <i>Journal of Geophysical Research Oceans</i> 114 (C3). https://doi.org/10.1029/	1255
	J. D. Pietrzak. 2016. "An Efficient Semi-Implicit Subgrid Method for Free-Surface Flows on Hierarchical Grids." International Journal for Numerical Methods in Fluids	2008JC005113. Zhang, Ying, and Mohammad Reza Najafi. 2020. "Probabilistic Numerical Modeling of Compound Flooding Caused by	1260
1195	80 (12): 715–741. https://doi.org/10.1002/fld.4172.	Tropical Storm Matthew Over a Data-Scarce Coastal	

Q9

Q10

Q11

1200

1205

1210

Powell, Mark D, and I. Ginis. 2006. Drag Coefficient Distribution and Wind Speed Dependence in Tropical Cyclones. Final Report to the National Oceanic and Atmospheric Administration (NOAA) Joint Hurricane Testbed (JHT) Program.

Rawls, Walter J, Lajpat R Ahuja, Donald L Brakensiek, Adel Shirmohammadi. 1992. Infiltration and Soil Water Movement. McGraw-Hill Inc.

Sanders, Brett F, Jochen E Schubert, and Humberto A Gallegos. 2008. "Integral Formulation of Shallow-Water Equations with Anisotropic Porosity for Urban Flood Modeling." Journal of Hydrology 362 (1-2): 19-38. https:// doi.org/10.1016/j.jhydrol.2008.08.009.

Santiago-Collazo, F'elix L, Matthew V Bilskie, and C Hagen. Scott. 2019. "A Comprehensive Review of Compound Inundation Models in Low-Gradient Coastal

Water Resources Research 56 (10): e2020WR028565. https://doi.org/10.1029/2020WR028565.

Zhang, Yinglong, and Antonio M Baptista. 2008. "SELFE: A Semi-Implicit Eulerian – Lagrangian Finite-Element Model for Cross-Scale Ocean Circulation." Ocean Modelling 21 (3-4): 71-96. https://doi.org/10.1016/j.oce mod.2007.11.005.

Zhang, Yinglong J, Fei Ye, Haocheng Yu, Weiling Sun, Saeed Moghimi, Edward Myers, Karinna Nunez, et al. 2020. "Simulating Compound Flooding Events in a Hurricane." Ocean Dynamics 70 (5): 621-640. https://doi. org/10.1007/s10236-020-01351-x.

Zilkoski, David B, John H Richards, and Gary M Young. 1992. "Results of the General Adjustment of the North American Vertical Datum of 1988." Surveying & Land Information Systems 52 (3): 133-149.

1270

1265

Q12

Appendix A. Measurement Locations

Table A1. Locations and identifiers NOAA tides and currents stations.

Identifier	Station ID	Name
1	8726724	Clearwater Beach, FL
2	8726520	Petersburg, Tampa Bay, FL
3	8726607	Old Port Tampa, FL
4	8726674	East Bay, FL
5	8726384	Port Manatee, FL

Table A2. Locations and identifiers for USGS observations during eta 2020. Locations also shown in Figure 2. Model results were explored via hydrographs (figure at selected water-level sensors with identifiers in the first column.

Identifier	Station ID	Identifier	Station ID	Identifier	Station ID
1	02299950	2	02300017	3	02300017
4	02300033	5	02300042	6	02300075
7	02300082	8	02300095	9	02300300
10	02300500	11	02300700	12	0230703
13	02301635	14	02301718	15	02301721
16	02301738	17	02301740	18	02301745
19	02301750	20	02301739	21	02306028
22	02306647	23	02307000	24	02307032
25	02307496	26	02307668	27	02307669
28	02307780	29	02308861	30	02308870
31	02308889	32	02308950	33	02309110
34	02309415	35	02309421	36	02309425
37	023060013				